PAPER • OPEN ACCESS

Cartilaginous spheroid-assembly design considerations for endochondral ossification: towards robotic-driven biomanufacturing

View the article online for updates and enhancements.

You may also like

Biofabrication

PAPER

Cartilaginous spheroid-assembly design considerations for endochondral ossification: towards robotic-driven biomanufacturing

Gabriella Nilsson Hall[1,2] (ID)**, Iene Rutten**[3]**, Jeroen Lammertyn**[3]**, Jens Eberhardt**[4]**, Liesbet Geris**[1,5,6] (ID)**, Frank P Luyten**[1,2,8] **and Ioannis Papantoniou**[1,2,7,8,*]

[1] Prometheus Division of Skeletal Tissue Engineering, KU Leuven, O&N1, Herestraat 49, PB 813, 3000 Leuven, Belgium
[2] Skeletal Biology and Engineering Research Center, Department of Development and Regeneration, KU Leuven, O&N1, Herestraat 49, PB 813, 3000 Leuven, Belgium
[3] Department of Biosystems, Biosensors Group, KU Leuven, Willem de Croylaan 42, Box 2428, 3001 Leuven, Belgium
[4] ALS Automated Lab Solutions GmbH, Jena, Germany
[5] GIGA in silico medicine, Université de Liège, Avenue de l'Hôpital 11—BAT 34, 4000 Liège 1, Belgium
[6] Biomechanics Section, KU Leuven, Celestijnenlaan 300C, PB 2419, 3001 Leuven, Belgium
[7] Institute of Chemical Engineering Sciences, Foundation for Research and Technology-Hellas, Stadiou 26504, Platani, Patras, Greece
[8] Co-senior authors.
[*] Author to whom any correspondence should be addressed.

E-mail: ioannis.papantoniou@kuleuven.be

Keywords: cartilaginous spheroids, bioassembly, endochondral ossification, biomanufacturing, tissue engineering

Supplementary material for this article is available online

Abstract

Spheroids have become essential building blocks for biofabrication of functional tissues. Spheroid formats allow high cell-densities to be efficiently engineered into tissue structures closely resembling the native tissues. In this work, we explore the assembly capacity of cartilaginous spheroids ($d \sim 150\ \mu$m) in the context of endochondral bone formation. The fusion capacity of spheroids at various degrees of differentiation was investigated and showed decreased kinetics as well as remodeling capacity with increased spheroid maturity. Subsequently, design considerations regarding the dimensions of engineered spheroid-based cartilaginous mesotissues were explored for the corresponding time points, defining critical dimensions for these type of tissues as they progressively mature. Next, mesotissue assemblies were implanted subcutaneously in order to investigate the influence of spheroid fusion parameters on endochondral ossification. Moreover, as a step towards industrialization, we demonstrated a novel automated image-guided robotics process, based on targeting and registering single-spheroids, covering the range of spheroid and mesotissue dimensions investigated in this work. This work highlights a robust and automated high-precision biomanufacturing roadmap for producing spheroid-based implants for bone regeneration.

1. Introduction

Modular tissue engineering strategies through the use of scaffold-free 'building blocks' have recently emerged as a novel paradigm for engineering functional tissue implants [1–3]. Assembly of different building block configurations have been explored, such as cell sheets [4], tissue strands [5], spheroids, microtissues and organoids [6–9]. The formation of these cellular building blocks is based on the inherent capacity of cells to aggregate and condense via adhesion molecules [10]. The native-like microenvironment allows the cellular structures to undergo crucial biological events such as condensation and extracellular matrix (ECM) production [2]. Through controlled differentiation, these living building blocks mature *in vitro* into microtissues and organoids which resemble native organs, also after assembly and fusion [6, 9]. Furthermore, the innate self-assembly properties of cellular building blocks enable fusion and a gradual increase in tissue size from microtissue (μm) to mesotissue (mm) and final macrotissue

(cm) length scale structures [2, 11]. Assembled tissues can be created as scaffold-free tissue implants [6, 9] or by hybrid biofabrication strategies with printed scaffolds [12–15]. These strategies enable modular biomanufacturing of complex tissue shapes through self-assembly of spheroids in prefabricated non-adherent molds [16–18] or via precise positioning using sacrificial support materials [6, 19]. In addition, further development of automated and scalable assembly processes using robotic systems is feasible [20, 21] but insights into building block fusion kinetics will be crucial to predict the assembly into functional tissues.

Hence, biofabrication of larger tissues using microtissues and organoids as 'building blocks' requires dedicated studies to provide understanding and defined parameters on the events occurring during spheroid assembly and fusion. These parameters should support the decision of spheroid culture time before scaffold-free assembly or integration with a scaffold [2, 22]. Previous studies demonstrated that spheroid fusion kinetics depends on cell type (e.g. human chondrocytes or human breast cancer cells), disturbance in their cytoskeleton [23], culture time in spheroid format [18] and number of cells per spheroid [24]. For example, spheres of sheep articular chondrocytes fused slower if matured longer individually before fusion [25]. Furthermore, the degree of matrix integration between the building blocks was shown to be affected by the time human bone marrow derived stromal cells were cultured as spheroids in chondrogenic media before assembly [8].

Cellular condensations are also key for engineering cartilage templates for indirect bone formation (endochondral ossification) which occurs during long bone development and fracture healing. Endochondral ossification starts with a condensation of progenitor cells followed by chondrocyte differentiation resulting in the formation of a cartilage template consisting of hypertrophic chondrocytes and ECM. The cartilage template is subsequently remodeled into bone [10, 26, 27]. In biofabrication, successful bone formation by recapitulation of endochondral ossification via cellular condensations has been achieved by applying various scaffold-free formats [9, 28, 29]. In the case of spheroids, the size typically ranges from 100 to 300 μm operating in dimensions that prevent detrimental diffusion limitations during lengthy differentiation protocols [4, 5, 7]. Recently, it was demonstrated that assemblies of $\sim$ 100 μm sized 'callus organoids' could form bone organs upon implantation at ectopic and orthotopic sites in a murine animal model. In the study, progressive secretion and maturation of cartilaginous ECM was observed during spheroid differentiation which resulted in chondrocytes reaching a prehypertrophic phenotype after 21 days in chondrogenic media [9]. These spheroids were assembled during 24 h before implantation but quantitative fusion capacity or longer fusion duration was not investigated.

In the current study, we explored the assembly of cartilaginous spheroids derived from human periosteum-derived cells (hPDCs) to investigate their fusion capacity and the influence of fusion duration on mesotissue outcome and endochondral bone formation *in vivo*. First, (a) spheroid fusion capacity was assessed by quantifying spheroid dual fusion and spreading kinetics. Next, (b) the effect of spheroid assembly duration (how early the fusion is occurring) and mesotissue size on the final tissue structure was described. Finally, (c) we provide a proof-of-concept on the feasibility of image-guided robotic biomanufacturing of spheroid-based implants. We suggest the use of these design considerations to dictate how subsequent spheroid-based biofabrication strategies should be tailored to create functional tissues.

2. Materials and methods

2.1. Cell expansion
Periosteal biopsies from nine donors were digested for cell isolation and two cell pools of hPDCs were created (29 $\pm$ 12 and 14 $\pm$ 3 years old) as previously described [30]. Briefly, the periosteal biopsies were washed and digested in type IV collagenase (440 units mg^{-1}, Invitrogen, BE) in growth medium (high-glucose Dulbecco's modified Eagle's medium (DMEM, Invitrogen, BE) supplemented with 10% fetal bovine serum (Hyclone), and an antibiotic–antimycotic solution (100 μg ml^{-1} streptomycin, 100 units ml^{-1} penicillin and 0.25 μg ml^{-1} amphotericin B, Invitrogen, BE). Next, the digested cells having similar growth kinetics and bone formation capacity were pooled together to create a cell pool. The cell pool was expanded until passage 9 in growth medium at 37 °C, 5% CO_2 and 95% humidity. Growth medium was changed three times per week until 90% confluency when the cells were harvested with TrypLE™ Express (Life Technologies, UK). All procedures were approved by the ethical committee for Human Medical Research (Katholieke Universiteit Leuven) and patients' informed consent forms were obtained (ML7861).

2.2. Agarose microwell formation
The agarose microwells were obtained by a double-molding procedure using soft lithography techniques. First, a 3 inch silicon wafer (Microchemicals, Newton, MA, USA) was rinsed and cleaned with acetone. This was followed by a second rinse with isopropanol and the wafer was dried with pressurized nitrogen. After rinsing, the wafer was exposed to 120 °C for 15 min to remove all possible water from the surface. Next, a layer of adhesion promoter was spincoated on the wafer at 3000 rpm for 30 s. On top of this preliminary layer, SU-8 2075 photoresist (Microchemicals, Newton, MA, USA) was spincoated at 1250 rpm for 60 s. The spincoating was followed by a softbake of 5 min at 65 °C and 45 min at 95 °C.

The wafer was subsequently patterned by exposure to UV-light (350 mJ cm^{-2}) through a photomask. This exposure was followed by a post exposure bake of 5 min at 65 °C and 15 min at 95 °C. Finally, the SU-8 was developed for 20 min using propylene glycol monomethyl ether acetate (PGMEA, Sigma Aldrich, Saint Louis, MO, USA). After rinsing with isopropanol, the SU-8 mold was hardbaked at 95 °C for 1 h. The resulting mold consisted of wells with a depth and diameter of 200 μm, as determined with a surface profilometer (Dektak 3030, Veeco, NY, USA). To produce the PDMS mold, the monomer and curing agent (Dow Corning, Midland, MI, USA) were mixed. After thoroughly mixing both components, the mixture was degassed and casted onto the SU-8 mold. After a 2 h bake at 65 °C this mixture solidified and could be removed from the SU-8 mold resulting in PDMS pillars. To create the microwells, 3% w/v UltraPure™ agarose (Thermo Fisher) was poured over the PDMS mold and let to cool down. The agarose microwells were punched out (1.8 cm^2) and placed in a 24-well plate and sterilized under UV before formation of spheroids.

2.3. Spheroid formation

A total of 500 000 hPDCs were drop-seeded per agarose well-insert containing 2000 microwells and the cells were allowed to sediment into the microwells resulting in approximately 250 cells/microwell. The non-adherent agarose microwells allowed cells to only adhere to each other resulting in the formation of cellular aggregates which subsequently self-condensed into spherical structures, as previously demonstrated with confocal microscopy [9]. Spheroids were differentiated towards cartilaginous microtissues in a chemically defined chondrogenic medium (CM) composed of LG-DMEM (Gibco) supplemented with 1% antibiotic-antimycotic (100 units ml^{-1} penicillin, 100 mg ml^{-1} streptomycin and 0.25 mg ml^{-1} amphotericin B), 1 mM ascorbate-2 phosphate, 100 nM dexamethasone, 40 μg ml^{-1} proline, 20 μM of Rho-kinase inhibitor Y27632 (Axon Medchem), ITS+ Premix Universal Culture Supplement (Corning) (including 6.25 μg ml^{-1} insulin, 6.25 μg ml^{-1} transferrin, 6.25 μg ml^{-1} selenious acid, 1.25 μg ml^{-1} bovine serum albumin, and 5.35 μg ml^{-1} linoleic acid), 100 ng ml^{-1} BMP-2 (INDUCTOS®), 100 ng ml^{-1} GDF5 (PeproTech), 10 ng ml^{-1} TGFβ1 (PeproTech), 1 ng ml^{-1} BMP-6 (PeproTech) and 0.2 ng ml^{-1} FGF-2 (R&D systems) [31]. Half of the media was carefully exchanged every 3–4 days.

2.4. Confocal imaging and semi quantification of f-actin

Spheroids were flushed out from their microwells and fixed in 4% paraformaldehyde (PFA) for 1 h at room temperature. Next, cell nuclei and filamentous actin (F-actin) were stained with 2.5 μg ml^{-1} 4′, 6-diamidino-2-phenylindole (Invitrogen) and 0.8 U ml^{-1} Alexa Fluor 488® phalloidin (Invitrogen) during 1 h at room temperature. Stained spheroids were imaged with an inverted laser scanning fluorescence confocal microscope ZEISS LSM 510 META (Cell imaging core facility of KU Leuven) with 1 μm thick slices using an argon ion 488 nm and MaiTai® laser.

2.5. Dual fusion and spreading assay

Dual spheroid fusion was performed in MicroTissues® 3D Petri Dish® (Sigma-Aldrich, BE) for 12-well plate. The manufacturer's instructions were followed to create 256 agarose microwells with 400 μm diameter and 800 μm depth. Next, approximately 500 spheroids were seeded into the 12-well plate that was placed in a well-plate incubator for imaging [32]. Microwells containing two spheroids were selected and imaged (10× magnification) for 24 h taking one picture every 10 min. The projection area and aspect ratio (AR) of the fusing spheroids of each frame was quantified using 'Find edges' and 'Analyze Particles' in ImageJ [33].

Spheroids of different maturity (1, 7, 14 or 21 days) were flushed out and 2 ml fresh CM was added. Next, the spheroid suspension was distributed in adherent 12 well plate (1 ml per well) and placed in a live cell monitoring system including a microscope and well plate incubator (OKOlab Top Stage Incubator) as described elsewhere [32]. The spheroids were imaged with a SC30 Colour Camera (Olympus) and 10× magnification during 20 h. The first time-point was used to define the projection area of the spheroids using Thresholding and 'Analyzing Particles' in ImageJ while the 20 h' time-point was used to quantify the spreading area using manual drawing and the ROI manager in ImageJ [33]. The spreading capacity was defined as fold change: the area after 20 h divided by initial spheroid projection area and the relative maximum displacement after 20 h (μm) was calculated according to $\frac{\text{major}(20\,\text{h})\mu m - \text{major}(0\,\text{h})\mu m}{2}$.

2.6. Multifusion of spheroids into mesotissues

Macrowells with a diameter of 2 mm were produced in-house with 3% w/v UltraPure™ agarose (Thermo Fisher) and sterilized under UV. Approximately 2000 or 1000 spheroids of 1, 7, 14 or 21 days maturity were pipetted into the macro-well with 40 μl of CM, let to sediment for 30 min at 37 °C where after 1 ml CM was added. Half of the media was changed every 3–4 days until a total culture time of 22 days.

2.7. Gene expression analysis

Spheroids from one well (∼2000) were pooled together, washed in PBS and lysed in 350 μl buffer RLT (Qiagen) and 3.5 μl β-mercaptoethanol (VWR)

followed by vortexing. Fused constructs were lysed in the same lysing buffer using FastPrep® −24 system and Lysing Matrix S-tubes. Total RNA was isolated using QIAshredder (Qiagen) followed by RNeasy Mini Kit (Qiagen). RNA concentration and quality were assessed with NanoDrop 2000 (Thermo Scientific) and PrimeScript™ RT reagent kit (Takara) was used for complementary DNA synthesis. Quantitative real-time polymerase chain reaction was performed using SYBR® Green (Life Technologies) on Rotor Gene® 6000 (Qiagen) and relative differences in expression were calculated using the $2^{-\Delta\Delta Ct}$ method normalized to hypoxanthine phosphoribosyltransferase 1 (HPRT1) as housekeeping gene [34]. All protocols were performed according to the manufacturer's protocol.

2.8. *In vivo* implantation and quantification of mineralized tissue

The construct's autonomy to form bone tissue was evaluated with a subcutaneous mouse model. Mesotissues (1000 fused microtissues per mesotissue) were implanted subcutaneously in immune compromised mice (Rj:NMRInu/nu). Explants were taken out four weeks after implantation and fixed in 4% PFA for subsequent nano-computed tomography (nano-CT). Samples were scanned with e*x vivo* nano-CT (Pheonix Nanotom M®, GE Measurement and Control Solutions) for 3D quantification of mineralized tissue. Scans were performed at 60 kV, 140 μA and with diamond target, mode 0, 1 frame average, 0 image skip, 500 ms exposure time, 2400 images and a 0.2 mm aluminum filter resulting in a voxel size of 2 μm. CTAn (Bruker micro-CT, BE) was used for image processing and quantification of mineralized tissue based on automatic Otsu segmentation, 3D space closing and despeckle algorithm. Percentage of mineralized tissue was calculated with respect to the total explant volume (MV/TV). CTvox (Bruker micro-CT, BE) was used to create 3D visualizations of the mineralized tissue. All procedures on animal experiments were approved by the local ethical committee for Animal Research, KU Leuven and the animals were housed according to the regulations of the Animalium Leuven (KU Leuven).

2.9. Histochemistry and immunohistochemistry

After nano-CT analysis, the explants were decalcified in ethylenediaminetetraacetic acid (EDTA)/PBS (pH 7.5) for 10 days at 4 °C followed by paraffin embedding. Samples were sectioned at 5 μm for subsequent alcian blue and safranin O staining according to previously described protocols [7]. Picrosirius red staining was performed by deparaffinization in Histo-Clear (national diagnostics, USA) and hydration followed by nuclei staining with Weigert's haematoxylin (Merck), washing in tap water, picrosirius red staining (0.1%, Sigma-Aldrich) for 1 h, washed in acidified water, dehydration and mounting. The stained

slides were imaged with Leica M165 FC microscope (Microsystems, BE) with bright-field and polarized light.

2.10. Image-guided robotic spheroid handling

Image-guided robotic spheroid picking and deposition was executed using the CellCelector™ (ALS GmbH, DE). The CellCelector™ consists of an inverted microscope (CKX41, Olympus) with a CCD camera system (XM10-IR, Olympus), a robotic arm with a capillary and an automated stage for well plates [35]. Single spheroids were picked from their agarose microwells (3% w/v UltraPure™ agarose, Thermo Fisher) by aspirating 0.5 μl with 1% speed using a capillary with an inner diameter of 150 μm. Next, the spheroids were deposited via robotic dispensing into a pre-targeted agarose microwell. In addition to single spheroids, five spheroids were picked with the same capillary using 0.15 μl of aspiration with 1% speed for each spheroid.

2.11. Statistical analysis

Statistical analysis was performed using GraphPad Prism 8 software (GraphPad Software, Inc., La Jolla, CA) and represented as mean $\pm$ S.D. if nothing else was noted. Analysis of Variance followed by Tukey post hoc test was used to find the significant differences between the means of the different groups with $p < 0.05$: *, $p < 0.01$: ** and $p < 0.001$: ***.

3. Results

3.1. Spheroids form cartilaginous microtissues

hPDCs were seeded onto non-adherent microwells (Ø 200 μm), leading to cell-cell attachment, self-aggregation and subsequent condensation (figure S1(A) (available online at stacks.iop.org/BF/13/045025/mmedia)). Side-view photo of the microwells and confocal images demonstrated that the cells had a spherical shape after seven days in culture (figures S1(A) and (B)). Chondrogenic differentiation was induced for 21 days to reach a pre-hypertrophic state as previously reported [9]. Spheroids were formed after one day in culture, although single cells were still discernible on the spheroid-surface (figure 1(A)). Over time, the spheroid surface became smoother, eliminating visible single cells. The spheroids grew slightly in size until day 14 (based on projection diameter) where after a decrease in size was monitored at day 21 (figure 1(B)). RNA-sequencing analysis of spheroids over time, previously reported by us [9], demonstrated up-regulation of chondrogenic transcription factors (TFs) (*SOX5, 6* and *9*) day 14 and day 21 and hypertrophic TFs distinctly up-regulated by day 21 (*RUNX3* and *MEF2C*) (figure 1(C)) [36]. Genes which encode collagens related to chondrogenesis (*COL2A1, COL9A1*) and more mature tissues (*COL10A1*) were significantly up-regulated on day 21. Furthermore, ECM proteins (DMP1, *SPP1* and

Figure 1. Chondrogenic maturation of cellular building-blocks. (A) Bright field images of spheroids over time. (B) Average spheroid diameter over time. Each data point represents individual spheroids, data pooled from four individual experiments, red lines show mean $\pm$ SD, one-way ANOVA followed by Tukey's post-hoc test. (C) Heat map demonstrating fold-change transcription of chondrogenic and hypertrophic gene markers (average of three samples). (D) Histological sections of spheroids stained with alcian blue. (E) Average normalized intensity of cortical phalloidin (F-actin) confocal images (5–8 spheroids per condition). (F) Width of normalized phalloidin intensity at 20% of maximal intensity. Graph shows violin plot with median and quartiles, each data point represents one spheroid, one-way ANOVA followed by Tukey's post-hoc test. Scale bars represent 50 μm. Significance was visualized with *: $p < 0.05$, **: $p < 0.01$ and ***: $p < 0.001$.

IBSP) associated with hypertrophic chondrocytes and osteogenic cells were up-regulated from day 14 and 21 (figure 1(C)). Alcian blue staining, specific for glycosaminoglycan-rich ECM demonstrated an expected increase in ECM overtime (figure 1(D)). These data indicated gradual maturation of spheroids into microtissues and callus organoids through both hypertrophic chondrocyte and osteogenic differentiation as described previously [9]. The gradual maturation allowed analysis of spheroids consisting of only cells (day 1 spheroids), combination of cells and ECM (day 7–14 microtissue) and with abundant

ECM (day 21 'callus organoids'). From here on in the results, all stages of spheroids will be described as spheroids.

To better define the change in spheroid surface over time that was detected with brightfield images, the cortical F-actin thickness was quantified for day 7, 14 and 21 spheroids (figure 1(E)). Day 1 spheroids were excluded since single cells were clearly present on the spheroid surface and no distinct cortical spheroid actin was present. A significantly thinner F-actin layer was detected between day 7 and 14 spheroids as well as between day 7 and day 21 (figure 1(F)).

3.2. Fusion and spreading capacity of cartilaginous spheroids is affected by time in culture

To assess the fusion capacity of chondrogenic spheroids, spheroids from each maturation stage (day 1, 7, 14 and 21) were dually assembled in agarose wells (400 μm in diameter). Attachment between all modules was detected after 1 h where after they gradually fused to form close to spherical or oval shapes (figure 2(A) and videos 1–4). Day 1 modules fused into a round sphere while day 21 modules resulted in an oval shape after 24 h of fusion. Viability staining demonstrated viable cells and the few dead cells were dispersed, hence indicating absence of necrotic cores within the fused spheroids (figure S1(C)). The fusion kinetics were defined by measuring the AR of the major and minor axis (figure 2(B)) and no significant difference in AR was detected between day 1, 7 and 14 modules. Nevertheless, day 1 modules continued to fuse towards a sphere after 15 h while day 7 and 14 modules attained a steady state after approximately 15 h (figure 2(C)). Interestingly, day 21 modules fused with a slower rate and reached a steady state even before forming a sphere demonstrating a significant difference after 20 h fusion as compared to day 1 spheroid duplets (figure 2(D)). The normalized duplet length after 20 h further indicated a significant difference between day 1 and 7 modules (figure S1(D)).

Moreover, alcian blue staining, specific for glycosaminoglycan rich ECM, revealed interior differences between fusions of different time-points (figure 2(E)). The two day 1 modules were barely visible after 24 h fusion while two different cores were clearly noticeable for day 7 and 14 modules and even more distinct in day 21 fusions. Sirius Red staining, specific for collagen fibers, demonstrated gradual collagen fiber maturation over time with two distinct module cores present already for day 7 modules (figures 2(F) and S1(E)). Although bright field images showed a close to spherical state after 24 h for day 1, 7 and 14 modules (figure 2(A)), the histological staining revealed that the mature ECM of the two modules was not fully fused (figures 2(E) and (F)). These data conclude that the differentiation and maturation of the spheroids affect the fusion kinetics and 21 days of maturation seem to delay fusion significantly although the modules were still attached to each other to form one tissue.

An important driving force during fusion of cellular spheroids is the capacity of cells to attach and migrate in between the modules. Additionally, cell contractility is expected to have an impact and the culture media used in this study contained the Rho kinase inhibitor Y27632 which suppress cytoskeletal rearrangements [37]. Absence of Y27632 in the culture media resulted in a larger AR after 20 h fusion of small spheroids (100 cells), indicating decreased fusion capacity (figure S1(F)). All other experiments were performed with addition of Y27632. Next, the
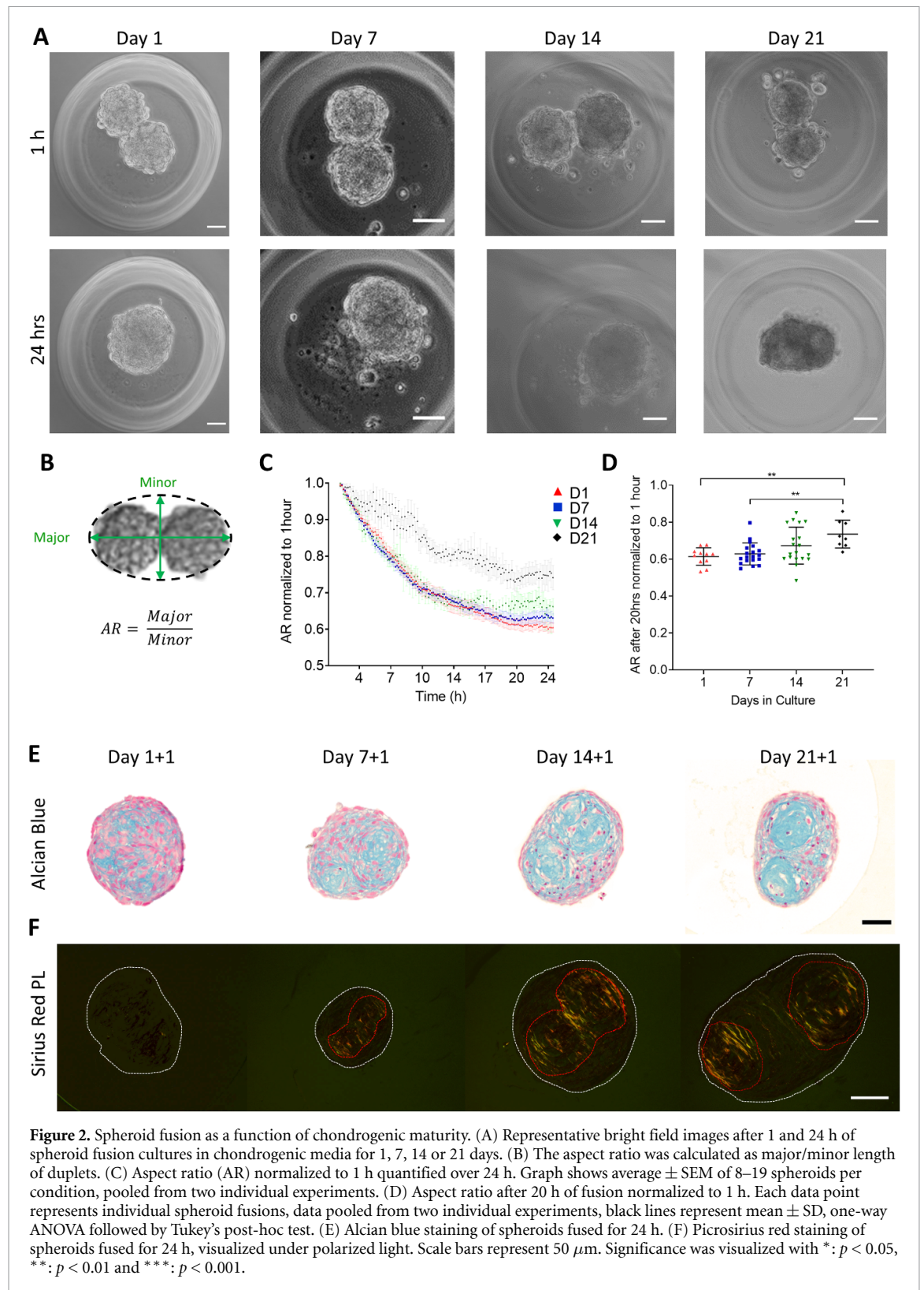
area of cells able to migrate out from the modules was characterized with a spreading assay. Spheroids of different maturity were seeded onto a cell adherent surface and imaged after 20 h to quantify the area that cells had spread from the initial spheroid (figure 3(A) and videos 5–8). The spreading area as compared to initial spheroid size was calculated to quantify the spread. As expected, day 1 spheroids exhibited largest spread area with more than 27 fold increase in area compared to their initial projection area (figure 3(B)). The spreading capacity decreased over time with 16, 8 and 5 fold spread area for day 7, 14 and 21 spheroids respectively. This would be expected since the spheroids day 7–21 contain a higher amount of ECM as compared to day 1. To address changes with regard to cellular migration, the relative maximum displacement over the 20 h of spreading was calculated (figure 3(C)). A continuous decrease in relative maximum displacement was detected for the following weeks. Taken together, the spreading assay demonstrates that the capacity of cells to spread from spheroids decrease over time in culture.

3.3. Assembly duration to direct mesotissue formation

Previous data demonstrated that spheroid maturation affects both fusion and spreading kinetics and that more mature modules fuse and spread slower (figures 2 and 3). These data indicate that the duration of module assembly also could affect the characteristics of a final construct or mesotissue. To study this, thousands of spheroids (~2000) were assembled after 1, 7 or 14 days in 24-well plates covered with agarose and cultured to fuse until day 22 (figures 4(A) and S2(A)). However, limited assembly was observed with a gradual decrease in fusion capacity from day 1, 7–14 modules after 1 week of fusion (figure S2(B)). To confine spheroids and promote active contact during fusion until day 22, a smaller non-adherent agarose well (2 mm in diameter) was constructed (figures 4(A) and S2(C)). With smaller agarose macrowells, all conditions resulted in relatively compact mesotissues (figure 4(B)).

The generated mesotissues were analyzed after a total culture time of 22 days. Polarized light of Sirius Red staining demonstrated a cortical collagen layer aligning the surface of D1-22 mesotissues and no spheroid shapes were detected within the constructs (figure 4(C)). In contrary, spheroid shaped patterns were seen at the border of D7- and D14-22 constructs, indicating limited spheroid fusion as depicted in the spreading assay. No or limited amount of collagen fibers were detected in the center of the D1-, D7- and D14-22 constructs while spheroid shaped collagen fibers were present throughout the D21-22 construct.
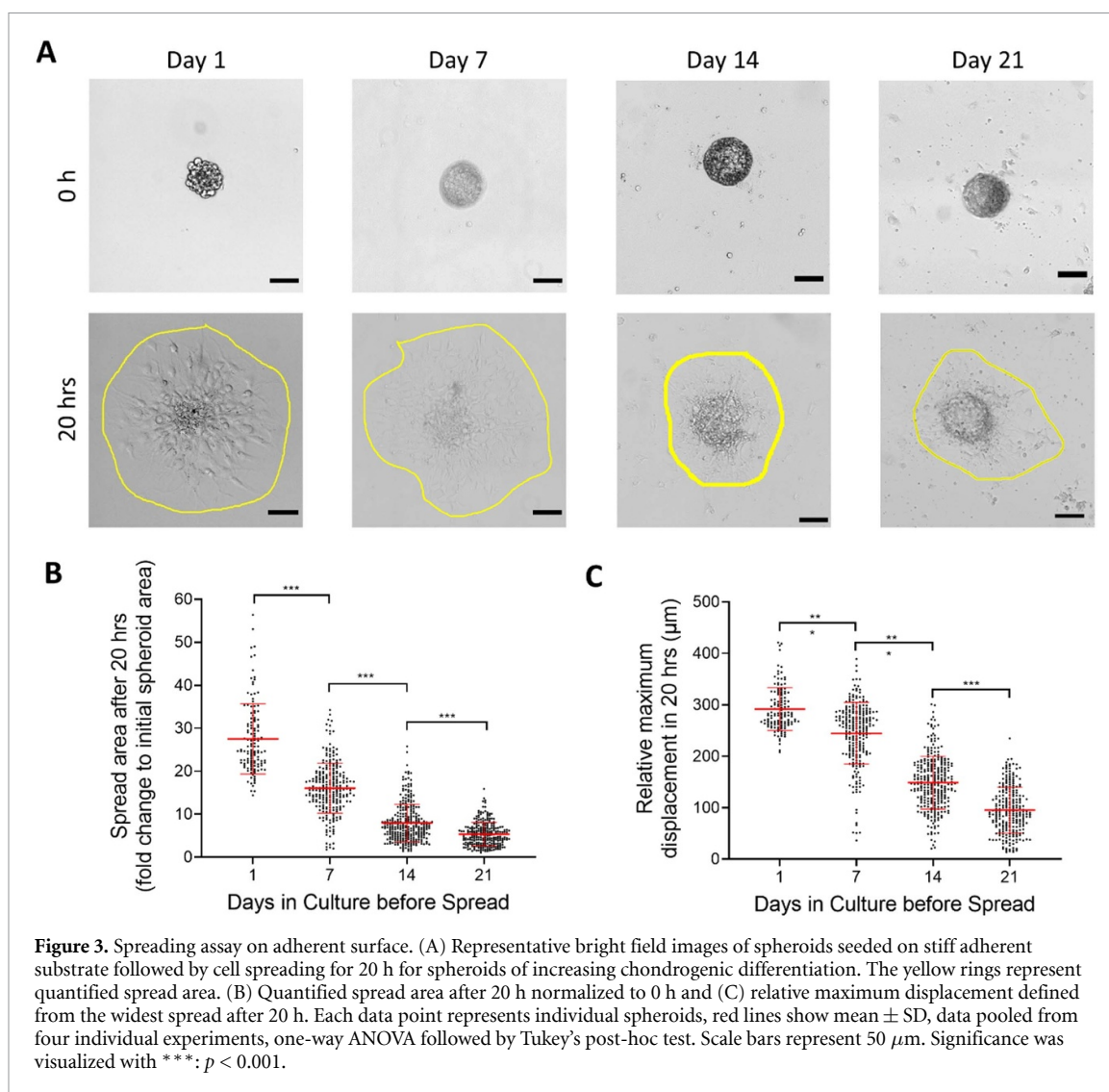
Safranin O staining (figure 4(D)) revealed a glycosaminoglycan (GAG) rich periphery with absence of or limited safranin O positive area in the center for the D1-, D7-, and D14-22 and Collagen type

Figure 2. Spheroid fusion as a function of chondrogenic maturity. (A) Representative bright field images after 1 and 24 h of spheroid fusion cultures in chondrogenic media for 1, 7, 14 or 21 days. (B) The aspect ratio was calculated as major/minor length of duplets. (C) Aspect ratio (AR) normalized to 1 h quantified over 24 h. Graph shows average $\pm$ SEM of 8–19 spheroids per condition, pooled from two individual experiments. (D) Aspect ratio after 20 h of fusion normalized to 1 h. Each data point represents individual spheroid fusions, data pooled from two individual experiments, black lines represent mean $\pm$ SD, one-way ANOVA followed by Tukey's post-hoc test. (E) Alcian blue staining of spheroids fused for 24 h. (F) Picrosirius red staining of spheroids fused for 24 h, visualized under polarized light. Scale bars represent 50 μm. Significance was visualized with *: $p < 0.05$, **: $p < 0.01$ and ***: $p < 0.001$.

2 (Coll 2) immunostaining demonstrated the same patterns (figure 4(E)). This indicates lack of differentiation, probably because of diffusion limitations and no significant difference in the thickness of the safranin O positive areas of D1-, D7- nor D14-22 constructs (456, 564 and 487 μm respectively, figure S2(D)), was detected. In contrast, D21-22 constructs were fused only 1 day and had safranin O positive area distributed throughout. These data depict that the constructs were too large for homogenous differentiation during long-term *in vitro* culture. The quantification of safranin O positive area resulted in an average thickness of 492 $\pm$ 92 μm for all samples. Hence, a mesotissue diameter of approximately 1 mm would be expected to allow differentiation throughout the constructs. This critical dimension (of approximately

Figure 3. Spreading assay on adherent surface. (A) Representative bright field images of spheroids seeded on stiff adherent substrate followed by cell spreading for 20 h for spheroids of increasing chondrogenic differentiation. The yellow rings represent quantified spread area. (B) Quantified spread area after 20 h normalized to 0 h and (C) relative maximum displacement defined from the widest spread after 20 h. Each data point represents individual spheroids, red lines show mean ± SD, data pooled from four individual experiments, one-way ANOVA followed by Tukey's post-hoc test. Scale bars represent 50 μm. Significance was visualized with ∗∗∗: $p < 0.001$.
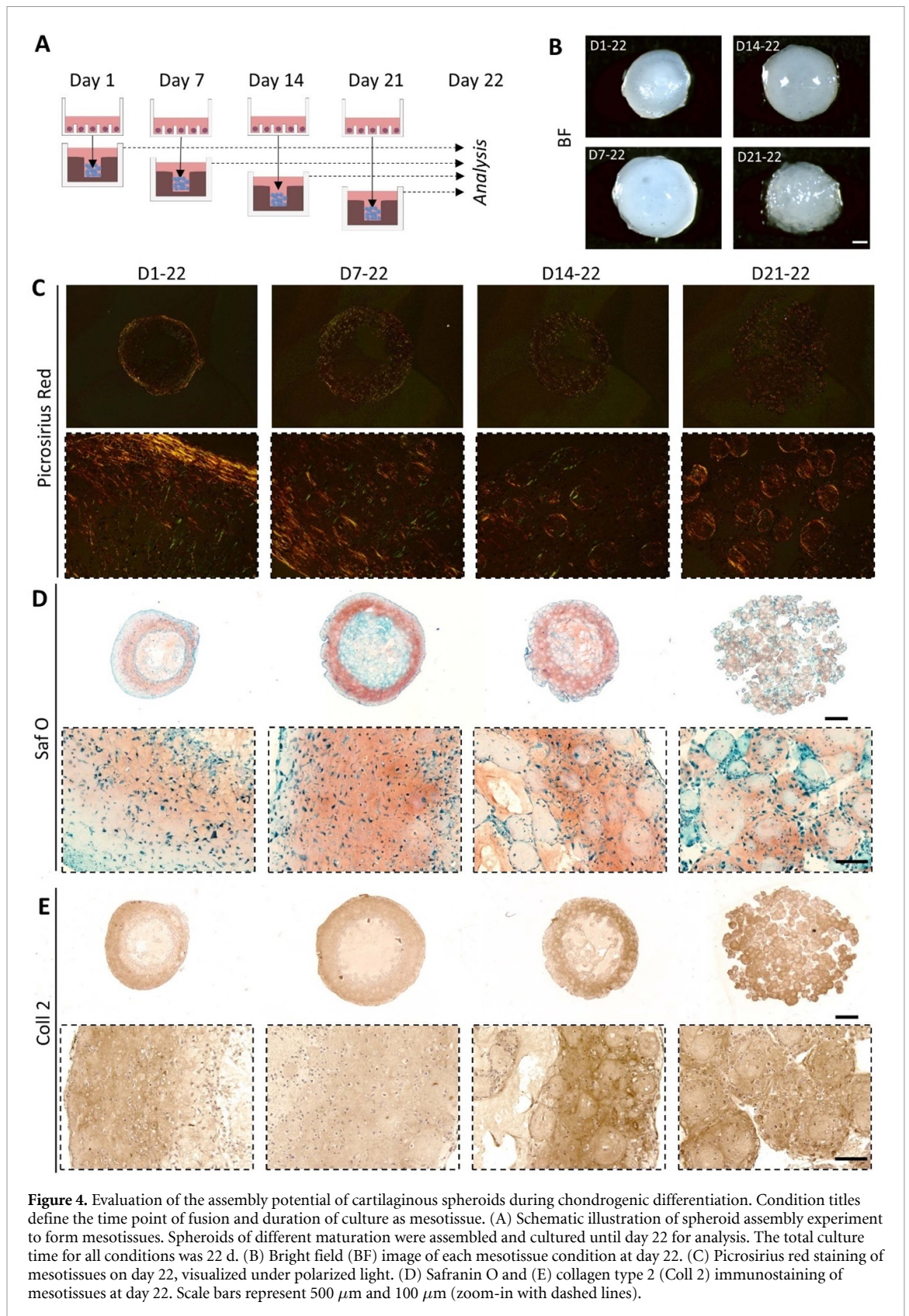
1 mm in diameter) was also identified in an *in silico* model of oxygen diffusion within spheroids (figure S2(E)). According to the *in silico* model, spheroids with a diameter of ⩽950 μm (corresponding to meso-tissues in figure 5) still have oxygen diffusion towards the center while spheroids with 2 mm in diameter (corresponding to mesotissues in figure 4) have a large area with oxygen deprivation (figure S2(F)). Hence, if the diameter exceeds this 1 mm threshold, diffusion limitations in the center of the mesotissues result in suboptimal chondrogenic differentiation as seen *in vitro* (figures 4(D) and (E)).

To avoid the consequences of diffusion limit-ations, smaller mesotissues (∼1000 spheroids/con-struct) were prepared (figure 5(A)). This resulted in mesotissues with an average diameter between 1.3 and 1.9 mm and average height of 0.78–0.96 mm (figures 5(B) and (C)). Histological staining showed safranin O positive staining throughout the major-ity of the construct confirming that diffusion limit-ations were restricted (figure 5(D)). No significant difference in gene expression for the chondrogenic marker *SOX9* nor the osteogenic and chondrocyte

hypertrophy markers *OSX* and *IHH* was detected (figure S3(A)) while a significant up-regulation in *COL2* and *COLX* mRNA was observed for D7-22 con-structs (figure S3(B)). Subsequently, D1-22, D7-22 and D21-22 constructs were implanted ectopically which resulted in mineralization and bone ossicle formation with bone marrow demonstrated with nanoCT (figures 5(E) and (F)) and safranin O stain-ing (figure 5(G)) after four weeks subcutaneous *in vivo* implantation.

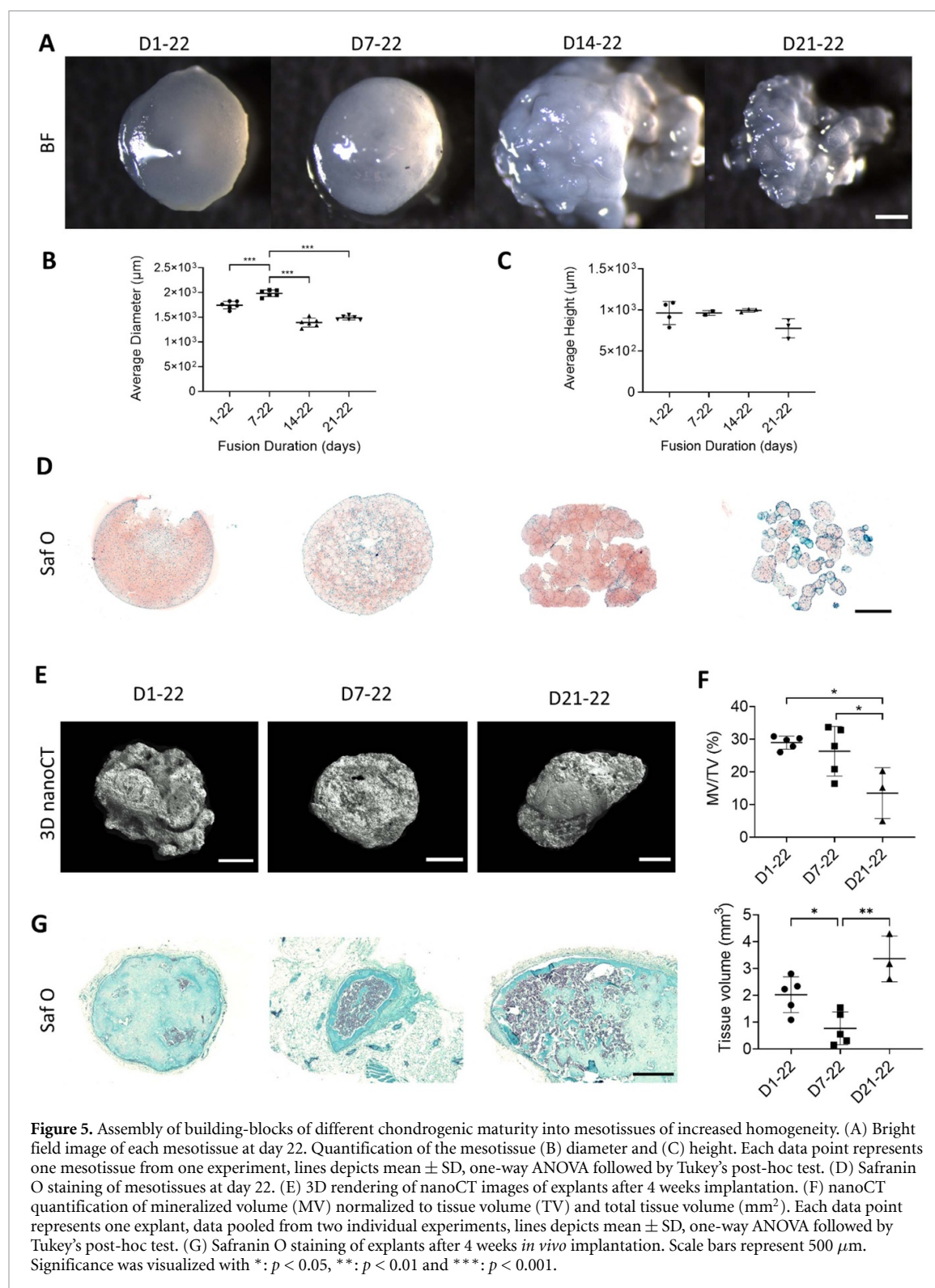### 3.4. Image-guided robotic spheroid assembly

The method for spheroid assembly that was described above, comprised manual bulk pipetting of thousands of modules simultaneously resulting in fusion of modules with varying characteristics. To enable auto-mated manufacturing of spheroid assembly-based implants, a robotic system namely the CellCelector™ [35] was applied in order to evaluate its capacity to target, pick up (through aspiration) and trans-fer spheroids in a controlled manner (figures 6(A) and S4(A)). Overview bright field pictures were created over the entire surface of 24 well plates to

Figure 4. Evaluation of the assembly potential of cartilaginous spheroids during chondrogenic differentiation. Condition titles define the time point of fusion and duration of culture as mesotissue. (A) Schematic illustration of spheroid assembly experiment to form mesotissues. Spheroids of different maturation were assembled and cultured until day 22 for analysis. The total culture time for all conditions was 22 d. (B) Bright field (BF) image of each mesotissue condition at day 22. (C) Picrosirius red staining of mesotissues on day 22, visualized under polarized light. (D) Safranin O and (E) collagen type 2 (Coll 2) immunostaining of mesotissues at day 22. Scale bars represent 500 μm and 100 μm (zoom-in with dashed lines).

visualize and locate each spheroid within the microwells (figures S4(C)). Spheroids of interest were manually selected in the software (figure 6(B)) and the robot positioned the needle above the selected spheroids. The spheroids were picked up in the needle (inne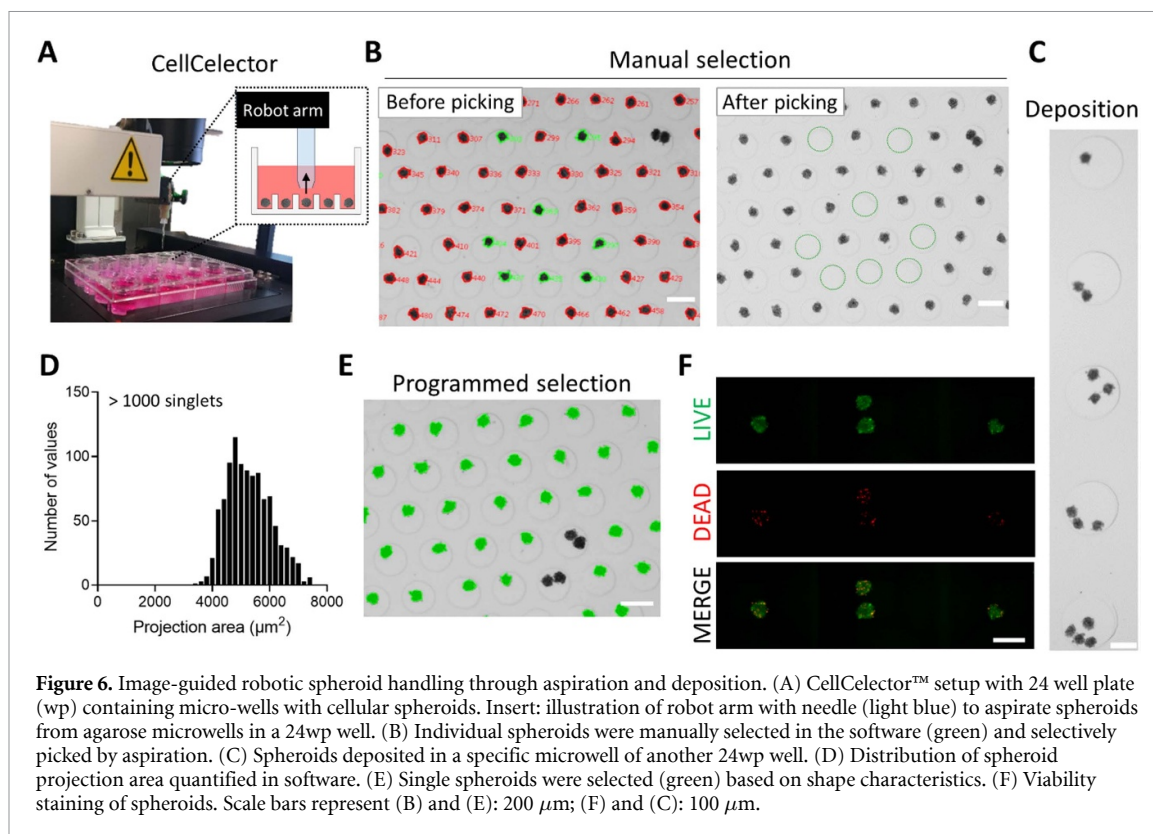r diameter of 150 μm) via aspiration with a success rate of 94.6% based on 56 recorded picks (figures 6(B) and S4(C)–(E) and video 9). Subsequently, aspirated spheroids were deposited from the needle into a non-adherent receiver microwell defined in the software and the spheroids remained within the targeted microwells based on gravitation

Figure 5. Assembly of building-blocks of different chondrogenic maturity into mesotissues of increased homogeneity. (A) Bright field image of each mesotissue at day 22. Quantification of the mesotissue (B) diameter and (C) height. Each data point represents one mesotissue from one experiment, lines depicts mean ± SD, one-way ANOVA followed by Tukey's post-hoc test. (D) Safranin O staining of mesotissues at day 22. (E) 3D rendering of nanoCT images of explants after 4 weeks implantation. (F) nanoCT quantification of mineralized volume (MV) normalized to tissue volume (TV) and total tissue volume (mm^2). Each data point represents one explant, data pooled from two individual experiments, lines depicts mean ± SD, one-way ANOVA followed by Tukey's post-hoc test. (G) Safranin O staining of explants after 4 weeks *in vivo* implantation. Scale bars represent 500 μm. Significance was visualized with *: $p < 0.05$, **: $p < 0.01$ and ***: $p < 0.001$.

(figure 6(C)). Parameters for each spheroid were logged to identify source well, position, shape characteristic and size allowing characterization of e.g. projection area of each individual spheroid as well as the whole spheroid population (figures 6(D) and S4(F)). Based on the spheroid identification and characterization, a programmed selection of microwells containing only one spheroid ('singlets') was done to avoid picking doublets (figure 6(E)). Fluorescent

imaging further enabled evaluation of viability for each spheroid (figure 6(F)). Additionally, picking of five spheroids at the same time was enabled by decreased aspiration volume (data not shown) as well as picking of larger spheroids with a diameter of 400 μm (figure S4(G)). The presented robotic setup demonstrated high throughput characterization of spheroids which were designated based on defined parameters (e.g. shape, size, viability) for selective

Figure 6. Image-guided robotic spheroid handling through aspiration and deposition. (A) CellCelector™ setup with 24 well plate (wp) containing micro-wells with cellular spheroids. Insert: illustration of robot arm with needle (light blue) to aspirate spheroids from agarose microwells in a 24wp well. (B) Individual spheroids were manually selected in the software (green) and selectively picked by aspiration. (C) Spheroids deposited in a specific microwell of another 24wp well. (D) Distribution of spheroid projection area quantified in software. (E) Single spheroids were selected (green) based on shape characteristics. (F) Viability staining of spheroids. Scale bars represent (B) and (E): 200 μm; (F) and (C): 100 μm.

picking and deposition in a pre-defined receiver well.

4. Discussion

In this study, we investigated the influence and limitations of bottom-up strategies for engineering modular spheroid-based cartilaginous implants for endochondral ossification. This approach holds great promise from both a biological perspective, as it provides a robust mechanism of action [9, 38], but also from the manufacturing perspective as it allows scalability and precision to be inbuilt in the final product. Finally, we provided evidence for the capacity to adopt fully automated bioprocesses tailored for the range of tissue dimensions investigated in this approach.

4.1. Cartilaginous spheroid fusion potential
We observed that the fusion capacity of cartilaginous spheroids decreased with increased maturation time *in vitro*. This was seen across scale with the AR of doublet spheroids as well as for assembly of thousands of spheroids (figures 2 and S2(B)). We attribute this to two reasons. (a) First, increased amounts of ECM per spheroid could contribute to this phenomenon and a decrease in fusion capacity correlated with increasing accumulation of ECM has previously been shown in a study of fusing spheroids from sheep articular chondrocytes [25]. Interestingly, in our study, apart from the day 1 spheroids (containing no ECM), distinct spheroid structure within the mesotissues was

maintained even for prolonged subsequent culture times (figure 4(C)). This data correlates with previous work which described integration of GAG-rich ECM between day 5 spheroids while fused day 7 spheroids had maintained boundaries between the spheroids [8]. It appears that fundamentally there is a distinct mechanism underlying spheroid fusion based on their maturation and 'rheological' properties and it remains to be further investigated how this might affect vascular invasion and rate of ossification, upon implantation.

(b) Spheroid self-assemblies are driven by highly contractile cells found at the periphery of spheroids [37, 39]. The thickness of the outer layer of cells in our study, defined by F-actin, per spheroid dropped during chondrogenic differentiation which could reflect the diminished power of fusion. We further assessed the cells capable of migrating out from spheroids by spreading of spheroids on a flat adherent surface [40]. A continuous decrease in relative maximum displacement (figure 3(C)) with increased spheroid maturation demonstrated a comparable trend as the normalized AR from the dual fusion assay (figure 2(D)) and the gradual fusion capacity during fusion of thousands of spheroids (figure S2(B)). Accordingly, the spreading assay could potentially serve as a real-time prediction assay regarding the fusion capacity of differentiated cartilaginous spheroids. As described in our study and others [41], the amount of ECM has an effect on building-block fusion but as in embryonic morphogenesis, presence of both cadherin and integrins and their communication with F-actin are also

involved in tissue self-assembly [24, 42–44]. Better understanding of the effect of these different parameters could be further addressed by using computational models of cellular aggregation and spheroid fusion [45].

4.2. Size limitations for spheroid-based cartilaginous templates

Spheroid size typically ranges from 100 to 300 μm in diameter to prevent the formation of detrimental diffusion limitations during lengthy differentiation protocols. We can expect two adverse outcomes related to diffusion: (a) detrimental outcomes such as increased cell apoptosis due to lack of nutrients or oxygen and (b) inadequate cell function or presence of ECM due to local lack of proper growth and differentiation factors [46, 47]. Moreover, these dimensions are highly dependent on the transient properties of differentiating cells and may vary from the type of tissue formed. In large bone marrow derived stromal cell (BMSC) spheroids, containing 60 000 cells, no hypoxic region was seen in the center while a hypoxic core was detected in spheroids containing at least 250 000 mesenchymal stromal cells (MSC)s [48], correlating with the number of cells to create mesotissues without fibrotic cores in our study (1000 spheroids = 250 000 seeded cells) (figure 5). Homogeneous differentiation is of importance since it has been reported that domains that are not positive of cartilaginous markers do not participate in the endochondral bone forming process leading to the presence of fibrous tissue structures [9, 38]. For BMSC-derived cartilaginous tissues, such inhomogeneities have been encountered in pellets and micromasses [9, 29, 49]. In our study, we defined a maximum diameter of progenitor derived cartilaginous tissue to 1000 μm that could be reached without compromising *in vitro* quality characteristics such as homogenous positivity for cartilaginous ECM markers. This dimension was also confirmed with a computational diffusion model based on oxygen (figure S2(E)). However, additional factors to oxygen concentration [50], such as nutrient and growth factor availability [47], are also of importance for the presence of necrotic or non-differentiated regions within tissue constructs. Regarding diffusion of growth factors, a more complex mechanism including active binding by cells through specific receptors and diffusion coefficients in cartilage can be envisioned. Moreover, the current study and computational model was based on static culture conditions but a dynamic culture environment could allow fabrication of even larger structures by enhanced mass transfer rates [51–53].

Finally, we observed that using the aforementioned design specifications, fused cartilage intermediate structures were able to form mineralized tissues upon implantation, independently of their fusion duration. Although no remarkable differences were observed after *in vivo* implantation, it appears that

a qualitative difference could be observed for the D7-22 and D21-22 mesotissues. In addition, a significant up-regulation of the collagens *COL2* and *COLX* mRNA was detected for D7-22 mesotissues (figure S3(B)), suggesting that their history before fusion might have affected the final outcome. Additional studies regarding the effect of fusion pre-history on bone forming potential *in vivo* is therefore of interest.

4.3. Image-guided robotic biomanufacturing for spheroid-based implants

For a viable and compliant clinical translation of cell-based products, the adoption of automated technologies has been acknowledged as a prerequisite [54]. Given the high promise of the recent *in vivo* outcomes observed through endochondral ossification, biomanufacturing technologies able to handle these tissue building blocks are of interest. Extrusion-based bioprinting [20, 55, 56] can be employed, however results to date indicate that structures with low cellular densities are obtained through this methodology while only low control over spheroid deposition can be achieved. A further disadvantage described for this approach is nozzle clogging when spheroids are bioprinted [11]. Robotics approaches such as the 'Kenzan' method [21], and 'biogripper' [57, 58] have been explored for scaffold-free handling of spheroids. However, the 'Kenzan' method requires homogenous spheroid sizes to enable proper fit onto the needle array [21] while the 'biogripper' is developed to handle larger building blocks (600–3400 μm) [57, 58]. Moreover, the existing techniques described to date lacked positional accuracy of spheroid deposition. Ayan *et al* recently demonstrated the use of aspiration for pick-up and positioning of spheroids [19, 59]. While this technique enabled gentle manipulation of spheroids, it was performed in a semi-automated fashion.

We demonstrated successful image-guided picking of spheroids through high precision spheroid aspiration and deposition. Image analysis allowed for high precision during the selection of targeted spheroids and was followed by precise transfer into a designated microwell. These operations were all logged end to end, enabling registering of spheroid history and may enable tracking of spheroid location within larger tissue structures. A future challenge of this approach will be the capacity to transfer the required volume of relevant tissues in reasonable timeframes, hence the system is currently low throughput, where the largest spheroid transferred in this study possessed a diameter of 400 μm. However, this could be mitigated by developing parallelized syringe systems while multiple spheroid aspiration also could be further explored. Moreover, combination with biomaterials [60, 61] or self-healing support hydrogels on the receiver well-plate could improve spatial organization during fusion of spheroids into tissue constructs [62]. The use of 'bioink' and 3D printing has also been

explored to create more elaborate shapes [63, 64], although the proximity of spheroids is of importance to allow spreading and fusion into a functional tissue. Further application of automated picking systems for module-based tissue engineering will permit the creation of complex tissues with both automation and precision.

5. Conclusion

We investigated design considerations of a scaffold-free, bottom-up biofabrication strategy in the context of endochondral ossification using cartilaginous spheroids. Design considerations related to the fusion of spheroids at different maturation degrees was investigated with regard to fusion capacity and assembly duration. Spheroid fusion and spreading capacity decreased with prolonged differentiation time and a critical *in vitro* construct dimension was defined to 1 mm, independent on fusion duration. Upon subcutaneous implantation, mineralization and bone organ formation was observed. Finally, a robotics driven biomanufacturing method for image-guided spheroid aspiration and deposition was presented, illustrating a way forward towards automated biomanufacturing of spheroid-based implants for tissue repair.

Data availability statement

The data that support the findings of this study are available upon reasonable request from the authors.

Author contributions

G N H, I P and F P L designed research; G N H, I R and J E performed research; J L and I R fabricated microwells; J E and G N H performed image-guided robotic experiments; G N H and I P analyzed data; G N H and I P wrote the manuscript draft and F P L, L G revised the manuscript. All authors reviewed the manuscript before submission.

Conflict of interest

Jens Eberhardt is co-founder of ALS automated lab solutions GmbH, Jena, Germany.

ORCID iDs

Gabriella Nilsson Hall ⓘ https://orcid.org/0000-0001-7803-652X
Liesbet Geris ⓘ https://orcid.org/0000-0002-8180-1445

References

[1] Ouyang L, Armstrong J P K, Salmeron-Sanchez M and Stevens M M 2020 Assembling living building blocks to engineer complex tissues *Adv. Funct. Mater.* **30** 1909009
[2] Laschke M W and Menger M D 2017 Life is 3D: boosting spheroid function for tissue engineering *Trends Biotechnol.* **35** 133–44
[3] Burdis R and Kelly D J 2021 Biofabrication and bioprinting using cellular aggregates and microtissues for the engineering of musculoskeletal tissues *Acta Biomater.* **126** 1–14
[4] McDermott A M *et al* 2019 Recapitulating bone development through engineered mesenchymal condensations and mechanical cues for tissue regeneration *Sci. Trans. Med.* **11** eaav7756
[5] Yu Y, Moncal K K, Li J, Peng W, Rivero I, Martin J A and Ozbolat I T 2016 Three-dimensional bioprinting using self-assembling scalable scaffold-free 'tissue strands' as a new bioink *Sci. Rep.* **6** 28714
[6] Skylar-Scott M A, Uzel S G M, Nam L L, Ahrens J H, Truby R L, Damaraju S and Lewis J A 2019 Biomanufacturing of organ-specific tissues with high cellular density and embedded vascular channels *Sci. Adv.* **5** eaaw2459
[7] Kim T G, Park S-H, Chung H J, Yang D-Y and Park T G 2010 Hierarchically assembled mesenchymal stem cell spheroids using biomimicking nanofilaments and microstructured scaffolds for vascularized adipose tissue engineering *Adv. Funct. Mater.* **20** 2303–9

[8] Bhumiratana S, Eton R E, Oungoulian S R, Wan L Q, Ateshian G A and Vunjak-Novakovic G 2014 Large, stratified, and mechanically functional human cartilage grown *in vitro* by mesenchymal condensation *Proc. Natl Acad. Sci. USA* **111** 6940–5

[9] Nilsson Hall G, Mendes L F, Gklava C, Geris L, Luyten F P and Papantoniou I 2020 Developmentally engineered callus organoid bioassemblies exhibit predictive *in vivo* long bone healing *Adv. Sci.* **7** 1902295

[10] Hall B K and Miyake T 2000 All for one and one for all: condensations and the initiation of skeletal development *Bioessays* **22** 138–47

[11] Mironov V, Visconti R P, Kasyanov V, Forgacs G, Drake C J and Markwald R R 2009 Organ printing: tissue spheroids as building blocks *Biomaterials* **30** 2164–74

[12] Leferink A, Schipper D, Arts E, Vrij E, Rivron N, Karperien M, Mittmann K, Van Blitterswijk C, Moroni L and Truckenmüller R 2014 Engineered micro-objects as scaffolding elements in cellular building blocks for bottom-up tissue engineering approaches *Adv. Mater.* **26** 2592–9

[13] Yajima Y, Yamada M, Utoh R and Seki M 2017 Collagen microparticle-mediated 3D cell organization: a facile route to bottom-up engineering of thick and porous tissues *ACS Biomater. Sci. Eng.* **3** 2144–54

[14] Levato R, Jungst T, Scheuring R G, Blunk T, Groll J and Malda J 2020 From shape to function: the next step in bioprinting *Adv. Mater.* **32** 1906423

[15] Carvalho D T O, Feijão T, Neves M I, Da Silva R M P and Barrias C C 2021 Directed self-assembly of spheroids into modular vascular beds for engineering large tissue constructs *Biofabrication* **13** 035008

[16] Livoti C M and Morgan J R 2010 Self-assembly and tissue fusion of toroid-shaped minimal building units *Tissue Eng.* A **16** 2051–61

[17] Dikina A D *et al* 2018 A modular strategy to engineer complex tissues and organs *Adv. Sci.* **5** 1700402

[18] Rago A P, Dean D M and Morgan J R 2009 Controlling cell position in complex heterotypic 3D microtissues by tissue fusion *Biotechnol. Bioeng.* **102** 1231–41

[19] Ayan B, Heo D N, Zhang Z, Dey M, Povilianskas A, Drapaca C and Ozbolat I T 2020 Aspiration-assisted bioprinting for precise positioning of biologics *Sci. Adv.* **6** eaaw5111

[20] Mekhileri N V, Lim K S, Brown G C J, Mutreja I, Schon B S, Hooper G J and Woodfield T B F 2018 Automated 3D bioassembly of micro-tissues for biofabrication of hybrid tissue engineered constructs *Biofabrication* **10** 024103

[21] Moldovan N I, Hibino N and Nakayama K 2017 Principles of the *Kenzan* method for robotic cell spheroid-based three-dimensional bioprinting *Tissue Eng.* B **23** 237–44

[22] Ovsianikov A, Khademhosseini A and Mironov V 2018 The synergy of scaffold-based and scaffold-free tissue engineering strategies *Trends Biotechnol.* **36** 348–57

[23] Susienka M J, Wilks B T and Morgan J R 2016 Quantifying the kinetics and morphological changes of the fusion of spheroid building blocks *Biofabrication* **8** 045003

[24] Olsen T R, Mattix B, Casco M, Herbst A, Williams C, Tarasidis A, Simionescu D, Visconti R P and Alexis F 2015 Manipulation of cellular spheroid composition and the effects on vascular tissue fusion *Acta Biomater.* **13** 188–98

[25] Omelyanenko N P *et al* 2018 Extracellular matrix determines biomechanical properties of chondrospheres during their maturation *in vitro Cartilage* **11** 521–31

[26] Kronenberg H 2003 Developmental regulation of the growth plate *Nature* **423** 332–6

[27] Vortkamp A, Pathi S, Peretti G M, Caruso E M, Zaleske D J and Tabin C J 1998 Recapitulation of signals regulating embryonic bone formation during postnatal growth and in fracture repair *Mech. Dev.* **71** 65–76

[28] Serafini M, Sacchetti B, Pievani A, Redaelli D, Remoli C, Biondi A, Riminucci M and Bianco P 2014 Establishment of bone marrow and hematopoietic niches *in vivo* by reversion of chondrocyte differentiation of human bone marrow stromal cells *Stem Cell Res.* **12** 659–72

[29] Mendes L F, Katagiri H, Tam W L, Chai Y C, Geris L, Roberts S J and Luyten F P 2018 Advancing osteochondral tissue engineering: bone morphogenetic protein, transforming growth factor, and fibroblast growth factor signaling drive ordered differentiation of periosteal cells resulting in stable cartilage and bone formation *in vivo Stem Cell Res. Ther.* **9** 1–13

[30] Eyckmans J, Roberts S J, Schrooten J and Luyten F P 2010 A clinically relevant model of osteoinduction: a process requiring calcium phosphate and BMP/Wnt signalling *J. Cell. Mol. Med.* **14** 1845–56

[31] Mendes L F, Tam W L, Chai Y C, Geris L, Luyten F P and Roberts S J 2016 Combinatorial analysis of growth factors reveals the contribution of bone morphogenetic proteins to chondrogenic differentiation of human periosteal cells *Tissue Eng.* C **22** 473–86

[32] Deckers T, Lambrechts T, Viazzi S, Hall G N, Papantoniou I, Bloemen V, Aerts J-M and Gullberg D 2018 High-throughput image-based monitoring of cell aggregation and microspheroid formation *PLoS One* **13** e0199092

[33] Schneider C A, Rasband W S and Eliceiri K W 2012 NIH Image to ImageJ: 25 years of image analysis *Nat. Methods* **9** 671–5

[34] Livak K J and Schmittgen T D 2001 Analysis of relative gene expression data using real-time quantitative PCR and the $2^{-\Delta\Delta\mathrm{CT}}$ method *Methods* **25** 402–8

[35] Nelep C and Eberhardt J 2018 Automated rare single cell picking with the ALS cellcelector™ *Cytometry* A **93** 1267–70

[36] Li J *et al* 2016 Systematic reconstruction of molecular cascades regulating GP development using single-cell RNA-Seq *Cell Rep.* **15** 1467–80

[37] Dean D M and Morgan J R 2008 Cytoskeletal-mediated tension modulates the directed self-assembly of microtissues *Tissue Eng.* A **14** 1989–97

[38] Scotti C, Piccinini E, Takizawa H, Todorov A, Bourgine P, Papadimitropoulos A, Barbero A, Manz M G and Martin I 2013 Engineering of a functional bone organ through endochondral ossification *Proc. Natl Acad. Sci. USA* **110** 3997–4002

[39] Youssef J, Nurse A K, Freund L B and Morgan J R 2011 Quantification of the forces driving self-assembly of three-dimensional microtissues *Proc. Natl Acad. Sci. USA* **108** 6993–8

[40] Beaune G, Stirbat T V, Khalifat N, Cochet-Escartin O, Garcia S, Gurchenkov V V, Murrell M P, Dufour S, Cuvelier D and Brochard-Wyart F 2014 How cells flow in the spreading of cellular aggregates *Proc. Natl Acad. Sci. USA* **111** 8055–60

[41] Hajdu Z, Mironov V, Mehesz A N, Norris R A, Markwald R R and Visconti R P 2010 Tissue spheroid fusion-based *in vitro* screening assays for analysis of tissue maturation *J Tissue Eng Regen Med.* **4** 659–64

[42] McMillen P and Holley S A 2015 Integration of cell-cell and cell-ECM adhesion in vertebrate morphogenesis *Curr. Opin. Cell Biol.* **36** 48–53

[43] Foty R A and Steinberg M S 2005 The differential adhesion hypothesis: a direct evaluation *Dev. Biol.* **278** 255–63

[44] Munjal A and Lecuit T 2014 Actomyosin networks and tissue morphogenesis *Development* **141** 1789–93

[45] Smeets B, Pešek J, Deckers T, Hall G N, Cuvelier M, Ongenae S, Bloemen V, Luyten F P, Papantoniou I and Ramon H 2020 Compaction dynamics during progenitor cell self-assembly reveal granular mechanics *Matter* **2** 1283–95

[46] Albro M B, Nims R J, Durney K M, Cigan A D, Shim J J, Vunjak-Novakovic G, Hung C T and Ateshian G A 2016 Heterogeneous engineered cartilage growth results from gradients of media-supplemented active TGF-β and is ameliorated by the alternative supplementation of latent TGF-β *Biomaterials* **77** 173–85

[47] Sarem M, Otto O, Tanaka S and Shastri V P 2019 Cell number in mesenchymal stem cell aggregates dictates cell stiffness and chondrogenesis *Stem Cell Res Ther.* **10** 10

[48] Murphy K C, Hung B P, Browne-Bourne S, Zhou D, Yeung J, Genetos D C and Leach J K 2017 Measurement of oxygen tension within mesenchymal stem cell spheroids *J. R. Soc. Interface* **14** 20160851

[49] Scotti C, Tonnarelli B, Papadimitropoulos A, Scherberich A, Schaeren S, Schauerte A, Lopez-Rios J, Zeller R, Barbero A and Martin I 2010 Recapitulation of endochondral bone formation using human adult mesenchymal stem cells as a paradigm for developmental engineering *Proc. Natl Acad. Sci. USA* **107** 7251–6

[50] Mohyeldin A, Garzón-Muvdi T and Quiñones-Hinojosa A 2010 Oxygen in stem cell biology: a critical component of the stem cell niche *Cell Stem Cell* **7** 150–61

[51] Bernhard J C, Hulphers E, Rieder B, Ferguson J C, Rünzler D, Nau T, Redl H and Vunjak-Novakovic G 2018 Perfusion enhances hypertrophic chondrocyte matrix deposition but not the bone formation *Tissue Eng.* A **24** 1022–33

[52] Vunjak-Novakovic G, Freed L E, Biron R J and Langer R 1996 Effects of mixing on the composition and morphology of tissue-engineered cartilage *AIChE J.* **42** 850–60

[53] Gupta P, Geris L, Luyten F P and Papantoniou I 2018 An integrated bioprocess for the expansion and chondrogenic priming of human periosteum-derived progenitor cells in suspension bioreactors *Biotechnol. J.* **13** 1700087

[54] Moutsatsou P, Ochs J, Schmitt R H, Hewitt C J and Hanga M P 2019 Automation in cell and gene therapy manufacturing: from past to future *Biotechnol. Lett.* **41** 1245–53

[55] Bulanova E A *et al* 2017 Bioprinting of a functional vascularized mouse thyroid gland construct *Biofabrication* **9** 034105

[56] De Moor L, Merovci I, Baetens S, Verstraeten J, Kowalska P, Krysko D V, De Vos W H and Declercq H 2018 High-throughput fabrication of vascularized spheroids for bioprinting *Biofabrication* **10** 035009

[57] Ip B C, Cui F, Tripathi A and Morgan J R 2016 The bio-gripper: a fluid-driven micro-manipulator of living tissue constructs for additive bio-manufacturing *Biofabrication* **8** 025015

[58] Blakely A M, Manning K L, Tripathi A and Morgan J R 2015 Bio-pick, place, and perfuse: a new instrument for three-dimensional tissue engineering *Tissue Eng.* C **21** 737–46

[59] Heo D N, Ayan B, Dey M, Banerjee D, Wee H, Lewis G S and Ozbolat I T 2021 Aspiration-assisted bioprinting of co-cultured osteogenic spheroids for bone tissue engineering *Biofabrication* **13** 015013

[60] Daly A C and Kelly D J 2019 Biofabrication of spatially organised tissues by directing the growth of cellular spheroids within 3D printed polymeric microchambers *Biomaterials* **197** 194–206

[61] Wu L, Zhou C, Zhang B, Lei H, Wang W, Pu X, Liu L, Liang J, Fan Y and Zhang X 2020 Construction of biomimetic natural wood hierarchical porous-structure bioceramic with micro/nanowhisker coating to modulate cellular behavior and osteoinductive activity *ACS Appl. Mater. Interfaces* **12** 48395–407

[62] Daly A C, Davidson M D and Burdick J A 2021 3D bioprinting of high cell-density heterogeneous tissue models through spheroid fusion within self-healing hydrogels *Nat. Commun.* **12** 1–13

[63] De Moor L, Fernandez S, Vercruysse C, Tytgat L, Asadian M, De Geyter N, Van Vlierberghe S, Dubruel P and Declercq H 2020 Hybrid bioprinting of chondrogenically induced human mesenchymal stem cell spheroids *Front. Bioeng. Biotechnol.* **8** 1–20

[64] Amaral A J R, Gaspar V M, Lavrador P and Mano J F 2021 Double network laminarin-boronic/alginate dynamic bioink for 3D bioprinting cell-laden constructs *Biofabrication* **13** 035045